



Atomic-scale study of the nano-cutting deformation mechanism of nickel-based single crystal superalloy containing Cr, Co, and γ/γ'

Zongxiao Zhu¹ · Donglei Luo¹ · Min Zheng¹ · Weihua Chen¹ · Xingchun Wei¹ · Dingfeng Qu¹ · Jingjing Zhang² · Jie Chen¹

Received: 19 January 2023 / Accepted: 16 March 2023 / Published online: 29 March 2023
© The Author(s), under exclusive licence to Springer-Verlag GmbH, DE part of Springer Nature 2023

Abstract

To study the cutting micromechanics of nickel-based single crystal superalloy containing γ/γ' two-phase structures and strengthening elements, a molecular dynamics method was used to establish a cutting model for nickel-based single crystal superalloy. The variation of machining force, shear strain, atomic displacement, and surface quality were analyzed in depth, and the effect of strengthening element content in the γ phase on the cutting behavior was investigated by comparing different models. It was found that the dislocation tangle is easily formed in the γ phase of nickel-based single crystal superalloy leading to increased machining forces, in addition, the coherent interface is stronger and can block the development of shear strain zones and the displacement of atoms. It is also found that the elastic recovery of γ phase is lower than that of γ' phase, resulting in the deepest part of the machined surface always appearing in γ phase. Finally, by studying the influence of the content of strengthening elements on the material, it is found that the strengthening elements Cr and Co in γ phase can promote the generation of dislocation tangle, and also enhance the strength of γ phase and coherent interface and improve the deformation resistance of the workpiece.

Keywords Molecular dynamics simulation · Nickel-based single crystal superalloy · Coherent interface · γ Phase · Reinforcement

1 Introduction

In recent years, nickel-based single crystal superalloys have been widely used in turbine blades of modern aero-engines due to their superior high-temperature strength and mechanical properties [1–4]. Owing to the unique γ/γ' two-phase structure, various alloy elements and single crystal properties make turbine blades can be used in complex and harsh environments [5, 6]. The microstructure of nickel-based single crystal superalloy is mainly formed by the crossover of matrix phase (γ phase) and strengthening phase (γ'), in which the disordered γ phase is an alloy phase composed of various elements and presents a grid shape, while the ordered γ' phase with cubic structure is embedded in the γ

matrix, and the volume ratio of the two phases is about 7:3, this special γ/γ' two-phase structure can limit the movement and development of dislocations [7–9]. The γ/γ' two-phase structure can limit the movement and development of dislocations. furthermore, the addition of solid solution strengthening elements Cr and Co in the alloy phase can improve the oxidation resistance and heat resistance of the material, as well as inhibit the precipitation of the harmful TCP phase [10–14]. With the development of industry, the machining accuracy of single crystal blades is becoming more and more demanding, and the way the material is removed determines the highest surface quality of the workpiece. High-speed cutting can significantly improve the quality of the machined surface, however, the microstructural changes that may be induced during the interaction between the machined surface and the cutting tool are not yet clear [15–18]. Moreover, the processing experiments carried out for nickel-based single crystal superalloy have obtained a surface roughness of less than 0.8 μm , at this time, the processing amount has reached the nanometer level, and the conventional technical means and processing theory can no longer explain [19]. Therefore,

✉ Zongxiao Zhu
zhuzongxiaolut@163.com

¹ School of Mechanical and Electrical Engineering, Lanzhou University of Technology, Lanzhou 730050, China

² School of Petrochemical Engineering, Lanzhou University of Technology, Lanzhou 730050, China

it is important to study the nano-cutting of nickel-based single crystal superalloy materials through the atomic scale.

To date, some results have been obtained in the experimental study of the processing of nickel-based single crystal superalloy. Qiu et al. [20]. demonstrated that the [110] crystal direction on the crystal plane of DD407 nickel-based single crystal superalloy (001) is the most desirable feed direction during milling. Zhang et al. [21]. elucidated that UVC combined with single crystal diamond tools can improve the machinability of nickel-based single crystal superalloy. Gao et al. [22]. performed micro-milling experiments on nickel-based single crystal superalloy DD98 and derived an energy storage model for recrystallization of the workpiece after plastic deformation, stating that the recrystallization probability is proportional to the shear force and temperature. Ming et al. [23]. found that a plastic deformation layer of about 2 μm appears on the grinded surface of DD5 alloy and a work-hardening layer of about 0.5 μm appears between the grinded surface and the plastic deformation layer. Xu et al. [24] conducted grinding tests on second-generation nickel-based single crystal superalloys under different grinding parameters and found that the grinding force decreased with increasing grinding speed and increased with increasing feed rate. Damage to materials is also the focus of processing research, and cracks can seriously affect the durability of the material structure [25]. Researchers can conduct crack particle modeling [26, 27], and then conduct finite element analysis with strong discontinuity embedded method (SDA) [28–30] and global crack element method (GCEM) [31–33] to solve a variety of static and dynamic problems [34–36].

However, when studying microscopic changes in advanced nickel-based single crystal superalloy, conventional machining experiments cannot provide a comprehensive and dynamic understanding of the microscopic changes inside the workpiece. In this case, a method that can extract atomic changes during transient processing is needed. In contrast, molecular dynamics simulations use the distribution pattern of atoms inside, the material, combined with the interaction forces between various elements, to construct simulation models that can accurately depict the material properties from the microscopic level. Based on the above method, it is possible to observe the complex and diverse dislocation and atomic motions inside the workpiece during machining [37, 38]. Hao et al. [39]. investigated the evolution of subsurface defects in silicon nitride tools cutting nickel-based single crystal superalloy by MD. Fan et al. [40]. found that solute atoms in nickel-based alloys can peg dislocations and hinder their movement. Hao et al. [41]. discussed the evolutionary mechanism of machined surface defects and material removal laws by cutting anisotropic nickel-based single crystal superalloy workpieces using silicon nitride tools through MD simulations. Lou et al. [42]. investigated the effect of changes in crystal orientation on subsurface

deformation during NBCS cutting. Xia et al. [43]. investigated the nano-cutting performance and mechanism of Ni/Ni₃Al phase interfacial structure by MD.

It has been found that the current processing experiments cannot observe the deformation of single crystals at the atomic scale, and the existing simulations are only conducted for single crystals with simple structures or two-phase models without reinforcing elements, which cannot accurately represent the deformation mechanism of real materials. Therefore, this study innovatively constructs a nickel-based single crystal cutting model containing γ/γ' structure, and then adds different strengthening elements (Cr and Co) to the γ phase to realistically reproduce the real structure and main elemental composition of the nickel-based single crystal superalloy. Based on the created cutting model, this paper systematically investigates the effects of γ/γ' two-phase structure and strengthening elements on the cutting behavior, revealing the nature of the cutting deformation behavior of nickel-based single crystal superalloy from the microscopic level, which is of great significance to the study of the machining behavior of nickel-based single crystal superalloy.

2 Methods

2.1 Simulation modelling

The molecular dynamics approach was used in this study. Cutting simulations were performed using a large-scale atomic/molecular parallel simulator [44]. The output of the simulations was post-processed and analyzed by OVITO visualization software [45]. The nano-cutting process of nickel-based single crystal superalloy containing strengthening elements and γ/γ' two-phase structure was systematically investigated. The model was developed as shown in Fig. 1. The model consists of a diamond tool and a nickel-based single crystal superalloy workpiece. Since the focus of this study is on the effect of strengthening elements and coherent interface to the machined workpiece, and since the hardness of diamond tools is much greater than that of nickel-based single crystal superalloy materials, the tools are treated as rigid bodies. The nickel-based single crystal superalloy material consists of two basic units: the γ phase is Ni–Cr–Co alloy and the γ' phase is Ni₃Al. The elemental components are shown in Table 1. Since the lattice constants of the two phases are close to each other, a coherent interface is formed at the junction of the two phases, as shown by \odot in Fig. 1. The simulation applies a constant speed of the tool and cuts the workpiece along the [100] Crystal orientation with a depth of cut of 26 Åm. Based on the created model, the cutting characteristics of nickel-based single crystal superalloy at the nanoscale can be studied in depth.

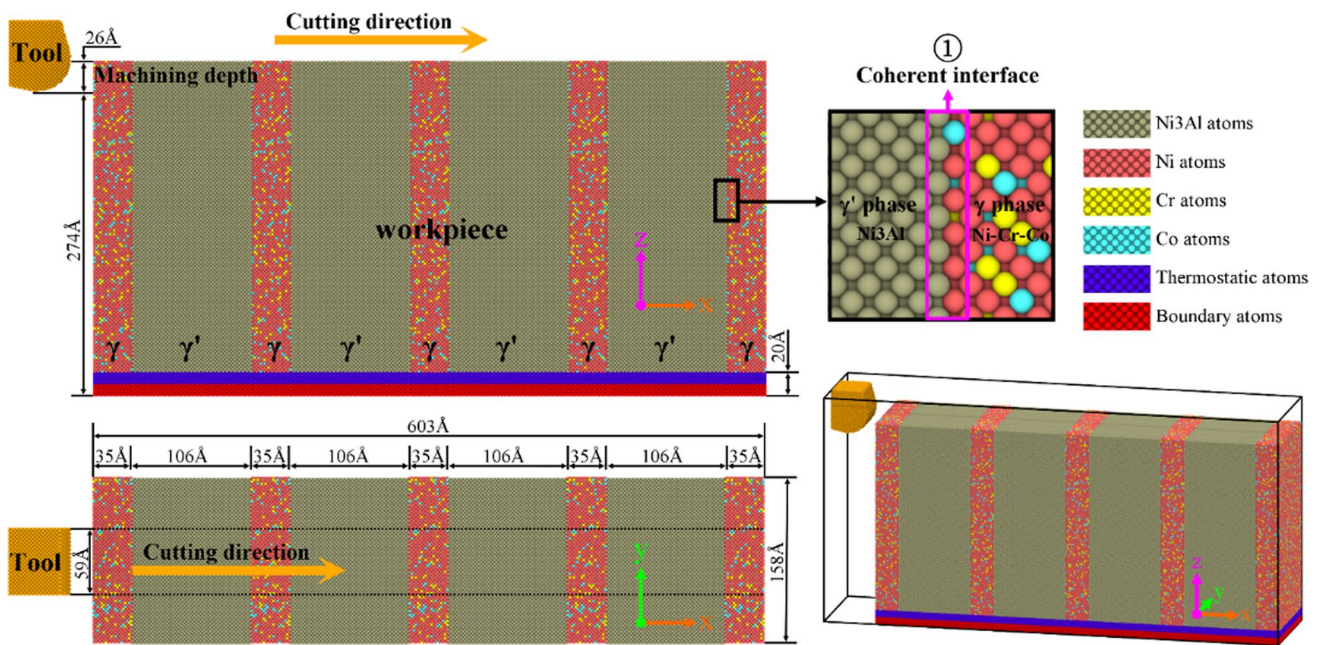


Fig. 1 Nickel-based single crystal superalloy cutting model

Table 1 Each element concentration component in simulation (wt.%)

Element	Ni	Al	Cr	Co
γ' phase region	75%	25%	0	0
γ phase region	82%	0	9%	9%

Table 2 lists the specific parameters of this simulation. The size of the workpiece is 603 Å × 158 Å × 300 Å and contains 2,631,269 atoms. The workpiece is divided into three regions, and the machining region is the Newtonian layer, which is the focus of the study of the cutting process and satisfies Newton's second theorem [46, 47]. The blue area in the middle is the thermostatic layer, which strictly follows the Nose–Hoover thermodynamic relationship and can ensure the constant temperature of the system [48]. The red area at the bottom is the boundary layer, which has a fixed effect on the whole workpiece and can ensure that the system does not move rigidly. In addition, to eliminate the boundary effect, the periodic

boundary is maintained in the X and Y directions and the free boundary in the Z direction [49, 50].

2.2 Selection of potential function

The key to ensuring the accuracy of molecular dynamics simulations lies in selecting the interatomic potential functions. A total of five types of atoms exist in this cutting simulation, of which (1) the interaction forces between diamond tool atoms (C–C) are described using the Tersoff potential [51].

(2) The interaction forces between the matrix atoms (Ni–Ni), (Cr–Cr), (Co–Co), (Al–Al), (Ni–Cr), (Ni–Co), (Ni–Al), and (Cr–Co) are described using the EAM potential. The total energy E_{tot} in the model is calculated as follows [52, 53].

$$E_{tot} = \frac{1}{2} \sum_{ij} \phi_{ij}(r_{ij}) + \sum_i F_i(\rho_i) \tag{1}$$

Table 2 Calculation parameters in MD friction simulation

Materials	Workpiece: Nickel-Base Single Crystal Superalloy	Tool: Diamond
Dimensions	Cubic: 60.3 nm × 15.8 nm × 30.0 nm	
Atomic number	2,631,269	32,569
Interatomic potential	Eam/fs Eam/alloy	Tersoff
Timestep	0.1 fs	
Initial temperature	300 K	
Grinding velocity	300 m/s	

$$\rho_i = \sum_{j \neq i} \rho_j(r_{ij}), \tag{2}$$

where, $F_i(\rho_i)$ represents the embedded energy induced by the embedding of atom i , ρ_i is the electron density of atom i , $\phi_{ij}(r_{ij})$ is the pair potential between atoms i and j , which are separated by a distance r_{ij} .

(3) The interaction forces between the diamond tool and the matrix atoms (C–Ni), (C–Cr), (C–Co), (C–Al), (Co–Al), and (Cr–Al) are described using the Morse potential, and the equation is as follows (3) [54].

$$U_{\text{Morse}}(r_{ij}) = D \left[e^{-2\alpha(r_{ij}-r_0)} - 2e^{-\alpha(r_{ij}-r_0)} \right], \tag{3}$$

where D is the cohesive energy, α is a constant determined by the material properties, r_{ij} is the distance between two atoms, r_0 is the distance at equilibrium, and the parameters are shown in Table 3 [55, 56].

3 Results and discussion

3.1 Study of mechanical properties and shear strain of workpieces

To accurately study the mechanical properties of the material throughout the cutting process, the normal force F_n and the tangential F_f between the tool and the workpiece are extracted, as shown in Fig. 2. It can be seen that with the increase of cutting distance, F_n and F_f gradually stabilize after the initial rapid growth. F_n and F_f fluctuate above and below 200 nN when entering the stabilization period, and the changing pattern is consistent. The fluctuation of machining force is determined by the complex two-phase structure in the nickel-based single crystal superalloy.

The development of dislocations during the cutting of nickel-based single crystal superalloy is mainly based on the bundle set and expansion of extended dislocations. When the motion of the extended dislocation is not obstructed, the machining force is smaller, as shown by a in Fig. 2. When

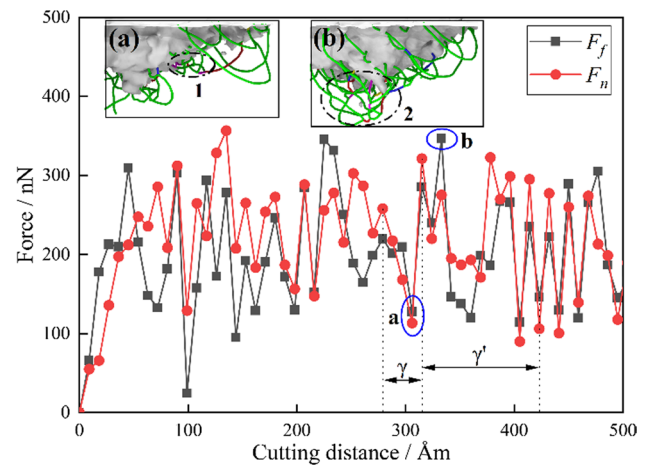


Fig. 2 Changes of normal force (F_n) and tangential force (F_f) during cutting of nickel-based single crystal superalloy

the tool cuts above the γ phase, the γ phase will produce pink Stair-rod sessile dislocations, as shown by 1 in Fig. 2a. As the tool advances, the green Shockley partial dislocation meets the Stair-rod sessile dislocations as it progresses forward. The two kinds of dislocations entangle with each other and promote the nucleation of the surrounding small dislocations, resulting in a continuous energy build-up in the region, causing F_n and F_f to increase continuously, as shown by a-b in Fig. 2. Finally, dislocation tangle is formed, as shown by 2 in Fig. 2b. The formation of a dislocation tangle hinders the development of dislocations, increases the deformation resistance of the workpiece, and improves the strength of the machined region.

The friction coefficient can reflect the machining state in different positions, and the equation is as follows (4).

$$\mu = F_f / F_n, \tag{4}$$

where: μ is the coefficient of friction, F_f is the tangential force, and F_n is the normal force.

Figure 3 shows the dynamic response curve of friction coefficient with the variation of cutting distance. It can be seen that the friction coefficient gradually stabilizes and fluctuates above and below a fixed value after the variation at the initial stage of machining, and we find that the fluctuation of friction coefficient is related to the evolution of defects, and the existence of coherent interface. First, under the action of the tool, a large crystal slip of the workpiece material occurs, accompanied by the generation of large structural defects and the consequent rapid increase in tangential forces, leading to an increase in the coefficient of friction, as shown by a in Fig. 3. However, when the defect in the large structure breaks and annihilates, the tangential force on the workpiece decreases, leading to a decrease in the coefficient of friction, as shown by b in Fig. 3. In addition, the presence of the

Table 3 Parameter setting of Morse potential function

Atomic type	Binding energy (D)	Elasticity modulus (α)	Atomic distance (r_0)
C–Ni	1.00392	1.98745	2.61994
C–Co	0.68810	1.73750	2.48630
C–Al	0.809282	1.8598	2.818508
C–Cr	1.034172	2.06355	2.617589
Co–Al	0.64770	1.68950	2.69700
Cr–Al	0.345413	1.36835	2.98603

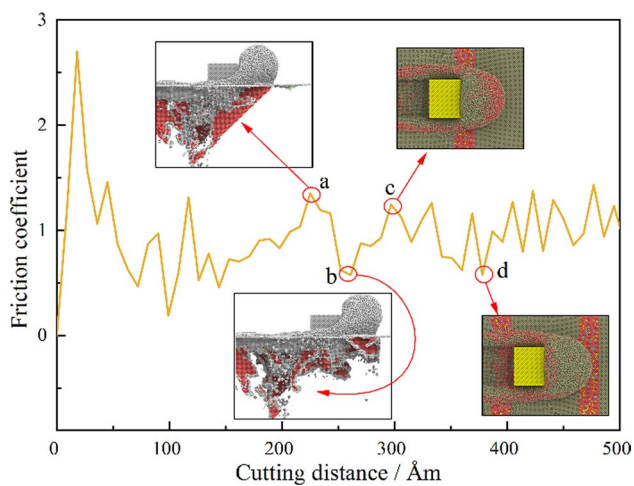


Fig. 3 Dynamic response curve of friction coefficient with cutting distance

interface also affects the fluctuation of the friction coefficient. When the tool is machining the coherent interface, the coherent interface with high strength will block the development of defects and form dislocation accumulation, resulting in an increase of the friction coefficient, as shown by c in Fig. 3. However, when the tool is machined to the interior of the γ' phase, the development of the defect is not blocked by the interface and the friction coefficient decreases with it, as shown by d in Fig. 3.

The shear strain reflects the relative deformation of the subsurface atoms of the workpiece during the cutting

process. The "Atomic strain" of "OVITO" can be used to observe the shear strain of the workpiece, as shown in Fig. 4. When the tool is machined in the γ' phase, the shear strain zone concentrates the machined surface and advances along an oblique upward 45° direction, as shown in Fig. 4a. However, when the tool approaches the γ phase, the subsurface develops a high strain zone along an oblique downward 45° , as shown by 1 and 2 in Fig. 4b. As the tool advances above the coherent interface, the strain region does not continue to expand, but large areas of high strain appear at the coherent interface and in the γ phase, as shown by 1 in Fig. 4c. It can be seen that the coherent interface can block the diffusion of the strain region, and the energy accumulates in front of the coherent interface. As the tool continues to advance, the coherent interface is disrupted, and the previously accumulated energy leads to a large strain region in the γ' phase, as shown by (d) in Fig. 4. When the tool is fully in the γ' phase, the machining force and energy are dispersed to the material within the phase and the strain region of the workpiece returns to a smaller range as shown by (e) in Fig. 4. At this point one machining cycle ends, and the tool continues to machine forward to near the coherent interface, and the strain region again develops along an oblique downward 45° into the next cycle, as shown by (f) in Fig. 4.

For the six positions in Fig. 4, count the number of atoms whose shear strain values is 0.025–0.05, 0.05–0.225 and more than 0.225, as shown in Fig. 5. It can be seen that in phases a-c, the atomic number of all ranges shows an increasing trend. This is due to the gradual approach of the tool to the γ phase during this process and the accumulation

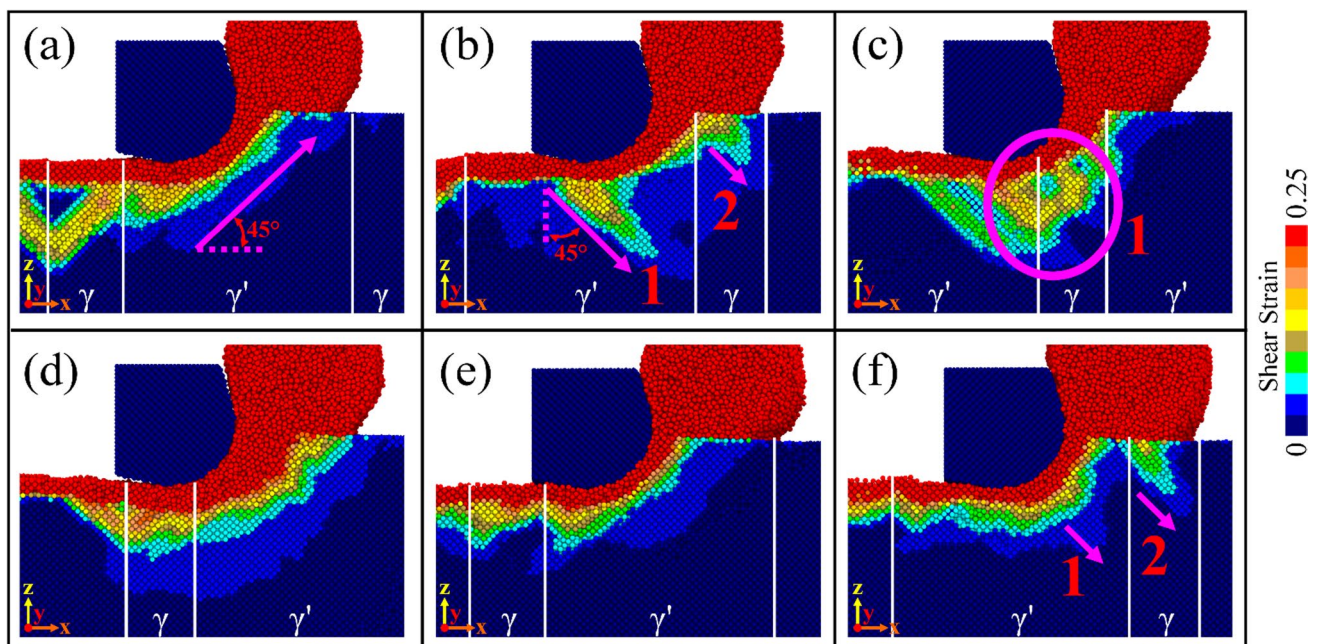


Fig. 4 Changes in subsurface atomic shear strain during processing

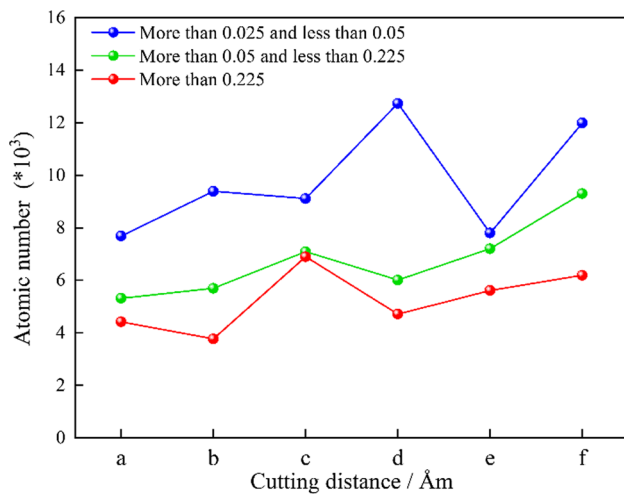


Fig. 5 Statistics of the number of shear strain atoms at different locations

of energy, which leads to an increase in the number of strained atoms. When the tool cuts to moment d, the number of low-strain atoms in the blue line increases rapidly, while the number of high-strain atoms in the red and green lines decreases. This is due to the release of the energy gathered by the workpiece in the initial moments when the tool enters the γ' phase, promoting an increase in the number of tiny strain atoms. When the machining reaches the e moment, the tool is entirely in the γ' phase, the accumulated energy has been consumed, the strain region is recovered and the number of blue low-strain atoms is again reduced.

To further analyze the strain pattern of the workpiece during cutting, the number of strain atoms during machining was counted, as shown in Fig. 6. The blue line counts the number of atoms with strain values in the interval 0.1–0.25. The blue strain curve increases smoothly and continuously with increasing cutting distance because some crystal defects remain inside the workpiece after machining and remain in a high-strain state. The black line counts the number of atoms with strain values in the 0.05–0.1 interval, and the curve gradually stabilizes after increasing at the beginning of machining, fluctuating back and forth within a certain range. This is because the region of shear strain gradually shrinks and disappears on the finished subsurface of the machining.

Analyzing a–f in Fig. 6 together with (a)–(f) in Fig. 4, it is found that the troughs a and e appear because the tool enters entirely into the γ' phase, and the range of shear strain is significantly reduced. However, when the tool is machined to the coherent interface, the strain region must expand, leading to a sharp increase in the number of strain atoms, as shown by b, d and f in Fig. 6. When the tool is machined to the γ phase, the strain region is concentrated on the location of the coherent interface and the γ phase and does not expand outward, as shown by (c) in Fig. 4. A trough in the number

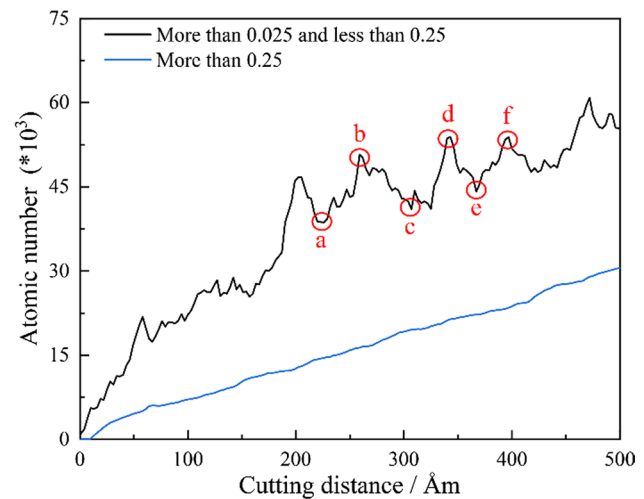


Fig. 6 The number of atoms of shear strain changes dynamically with cutting distance

of strain atoms also appears at this time, as shown by (c) in Fig. 6.

3.2 Study of atomic displacement and surface quality of workpieces

The material deformation caused by cutting can be directly reflected by atomic displacement. The atoms are color-coded by the magnitude of the material displacement during machining, as shown in Fig. 7. At the beginning of the machining, the tool cuts in the γ' phase, and a light blue displacement atom appears below the tool and is transmitted along an inclined downward direction of 45° , as shown by (a) in Fig. 7. When the tool enters the γ phase cutting, the deformation region of the workpiece increases rapidly, and the material on both sides of the tool moves along the directions 1 and 2 in Fig. 7b. As the tool continues to cut in the γ phase, the deformation region expands further until the tool leaves the γ phase and the first stage of deformation of the workpiece ends, as shown by (c) in Fig. 7. At this time, the workpiece appears irreversible fracture deformation, with the fracture lines L1 and L2 in Fig. 7c as the boundary, the displacement distance of the internal orange atoms is more than 5 \AA m and cannot be recovered, but the displacement distance of the atoms outside the fracture lines is within 3 \AA m and will gradually recover with time. Thus, it is found that cutting the γ phase can easily cause the overall deformation of the workpiece. When the tool cuts to the next γ phase it will enter the second phase of deformation, and the process is similar to the first phase. When the tool cuts to the γ_2 phase, the deformation region with larger displacement appears in the γ_2 phase, as shown by 1 in Fig. 7d and 2 in Fig. 7e. After the tool leaves the γ phase, the workpiece fractures along the fracture line L3 and L4 in the deformation

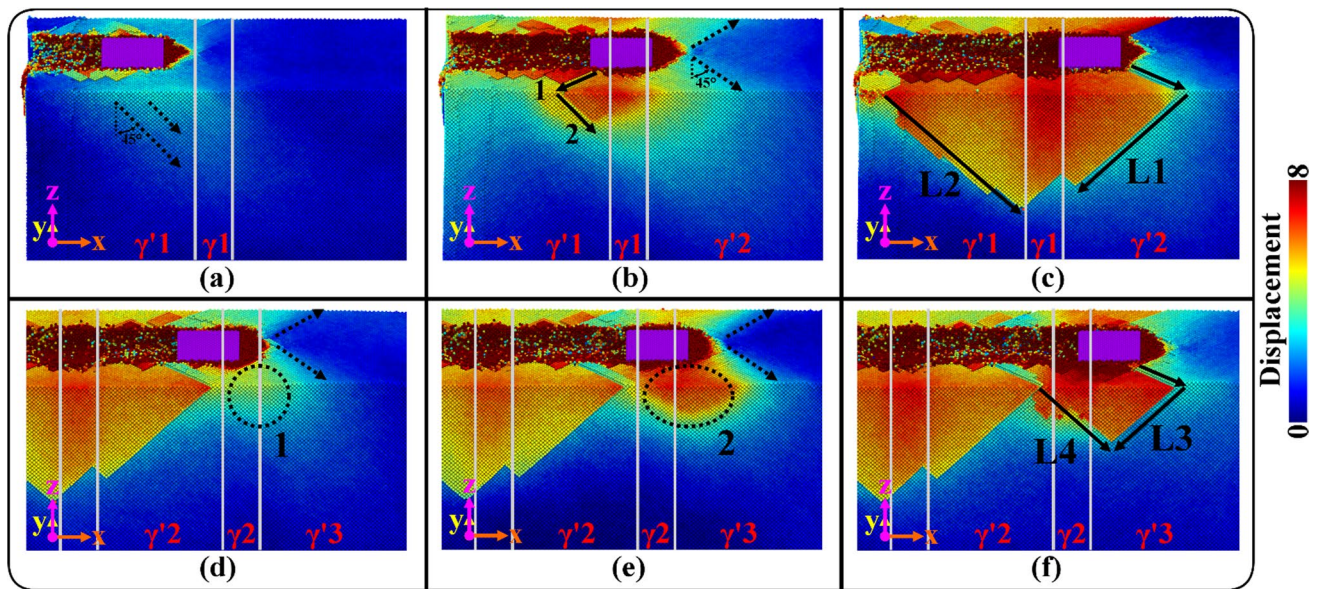


Fig. 7 Changes in displacement atoms during cutting. **a–f** Represent material morphologies at different cutting positions

region. It can be seen that the γ phase is hard and brittle, and the destruction of the γ phase always leads to irrecoverable fracture deformation of the workpiece.

To eliminate the influence of small displacements caused by atomic excitations, only the number of atoms displaced during the cutting process greater than 1.5 \AA was counted, as shown in Fig. 8. It was found that the machining process can be divided into three phases by the fluctuation of the curve. When the tool cuts into the γ phase, the number of displaced atoms increases rapidly, but when the tool leaves the γ phase, the number of atoms is not growing. This variation is consistent with the interpretation in Fig. 7.

To further investigate the deformation behavior of the material during the cutting process, the displacement vector analysis was performed on the workpiece while the tool was machined to a representative position, and the vector arrows were color-coded according to the magnitude of the vector, as shown in Fig. 9. When the tool is machined to the γ phase, the atoms in front of the tool will first move forward in a straight line after the force is applied, as shown by 1 in Fig. 9a. However, when the atoms encounter the coherent interface in their movement, they are blocked from moving forward in a straight line. This is due to the special mechanical properties of the coherent interface, which leads to its relatively high hardness. Atoms in front of the interface do not have enough energy to break through the interface and can only gradually accumulate energy as the tool advances, while the atoms move in the direction of the boundaries on both sides, as shown by 2 and 3 in Fig. 9a. As the tool keeps approaching the phase boundary, the atoms in front of the tool have accumulated

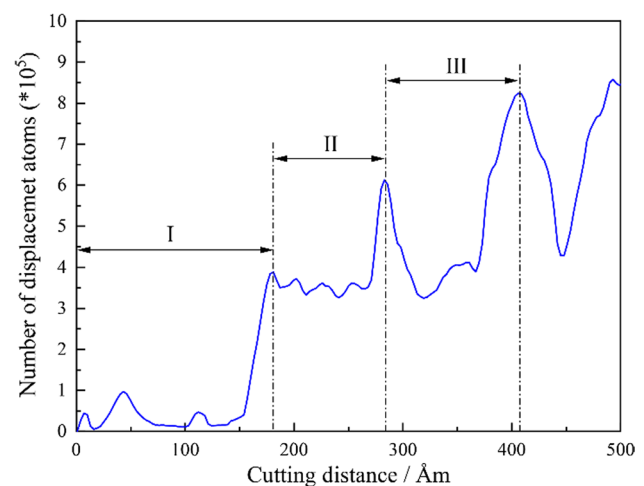
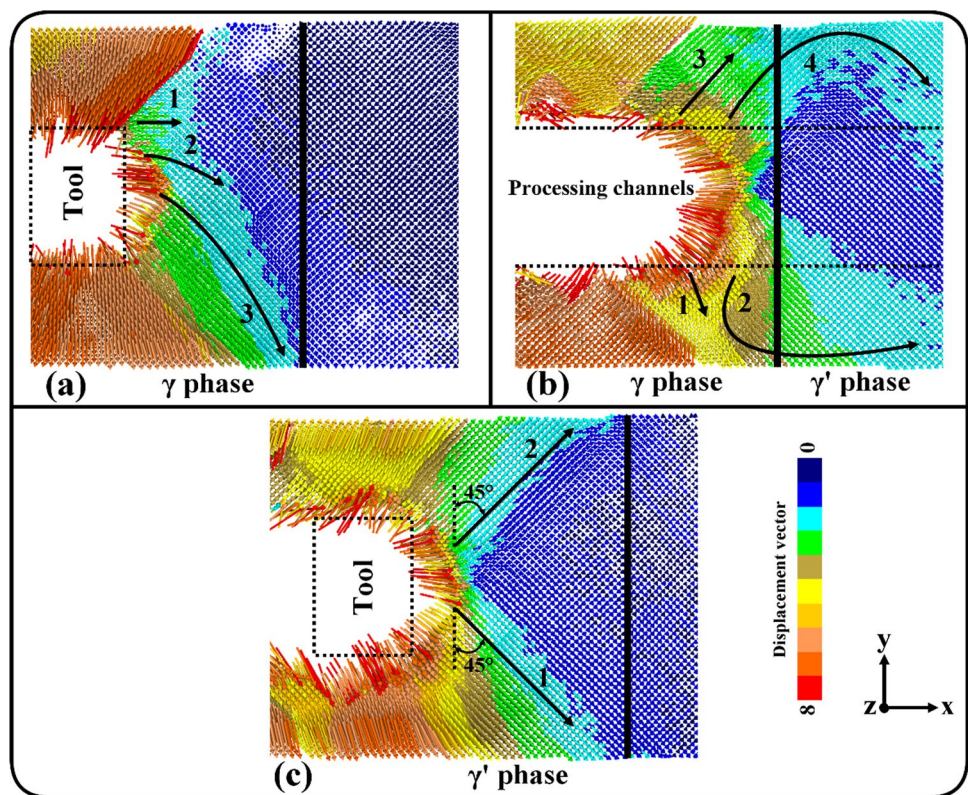


Fig. 8 The change of atoms with displacement is greater than the 1.5 \AA dynamic step response curve

a large amount of action energy and release some of it in the direction of the boundary, as shown by 1 and 3 in Fig. 9b. At the same time, a part of the atoms breaks through the coherent interface from the position at the boundary to transfer the action energy to the γ' phase, as shown by 2 and 4 in Fig. 9b. When the tool is fully in the γ' phase, the atoms in front of the tool move steadily in the direction of 45° on both sides, and the direction of motion at this point corresponds to the direction of the easiest slip plane of the FCC structured crystal, as shown by 1 and 2 in Fig. 9c. As can be seen above, the coherent interface at the junction of two phases can impede the movement of

Fig. 9 Different position displacement vector display



atoms inside the workpiece, which can improve the ability of plastic deformation of the workpiece.

The surface quality after machining is an important indicator of machining accuracy. A top view of the machined surface after cutting was obtained, as shown by (a) in Fig. 10. To facilitate analysis, the atoms were colored based on the height in the Z-direction, and the regions of each phase were divided. The black dashed ellipse in the figure marks the deepest part of the machined workpiece surface. It can be found that the darker blue area always appears in the γ phase, while the surface of the γ' phase is relatively higher. This is due to the weak elastic recovery of the γ phase and the stronger elastic recovery of the γ' phase.

After the tool cuts the workpiece, there will be an elastic force interaction between the atoms of the machined surface, and the potential energy from the elastic deformation is called elastic potential energy. For easy observation, the low potential energy atoms smaller than -3.6 are hidden. The subsurface potential energy distribution of the workpiece is obtained, as shown by (b), (c) and (d) in Fig. 10. It can be seen that when the tool cuts to the center of the γ' phase, it causes a large increase in the elastic potential energy inside the material, as shown by (b) in Fig. 10. When the tool extrudes the workpiece, there is an elastic interaction between the atoms, which results in a large amount of potential energy, as shown by 1 in Fig. 10b. However, when the tool is machined to the γ phase, there are no high

potential energy atoms inside the workpiece, but only at the location where the tool is in contact with the workpiece, as shown by 2 in Fig. 10c. Finally, by Fig. 10d, it is found that in the region after tool cutting, the γ' phase has more high potential energy atoms on the subsurface, and these high potential energy atoms continuously promote the elastic recovery of the γ' phase, as shown by 3 in Fig. 10d. However, the high potential energy atoms of the γ phase are very few, and only a very thin layer covers the subsurface, as shown by 4 in Fig. 10d. It can be seen that the elastic recovery of the γ phase is weak, and the machined surface depth is low. In comparison, the γ' phase has a stronger elastic recovery and high machined surface depth.

The number of potential energy atoms and chip number in the whole cutting process is counted in real-time, as shown in Fig. 11. The blue line counts the number of atoms with potential energy above -3.6 . The red line counts the number of chips on the machined surface. It can be seen that the growth trend of potential energy atoms and chips in the two phases is different, which is determined by the properties and strength of the materials in the two phases. When the tool cuts into the γ phase, there is a small decrease in the number of potential energy atoms, as shown by a–b in Fig. 11. But the chip production increases rapidly, as shown by d–e in Fig. 11. This is due to the relatively small elastic potential energy of the γ phase material. And the brittleness of the γ phase material

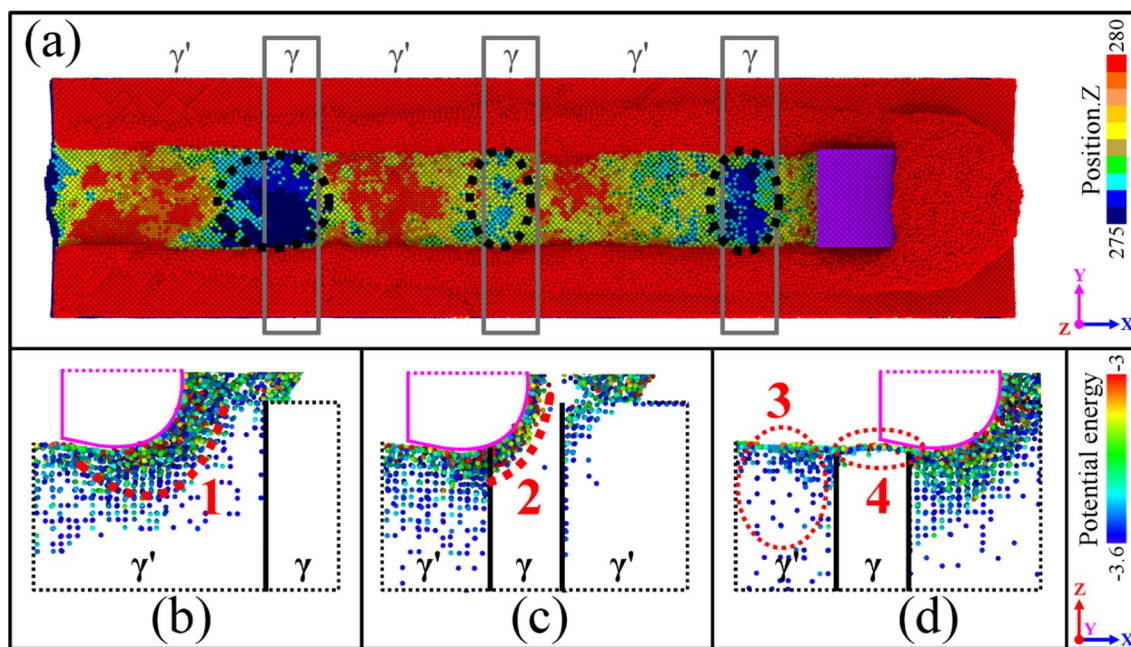


Fig. 10 **a** Depth distribution of machined surfaces. **b–d** Elastic potential energy distribution inside the workpiece during cutting

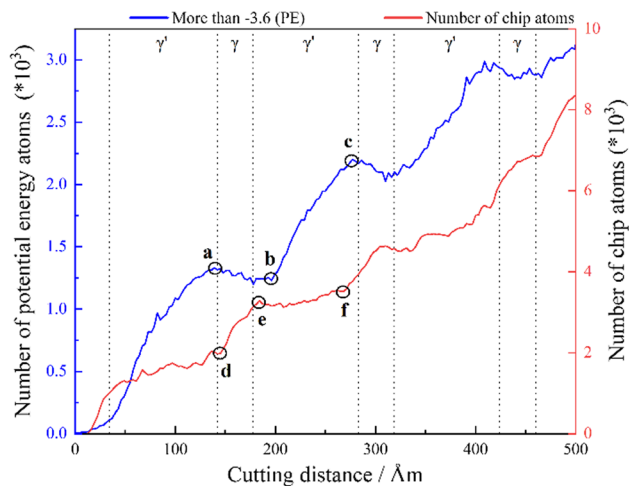


Fig. 11 Dynamic change curve of the number of potential energy atoms with cutting distance (blue curve). Dynamic change curve of chip atom number with cutting distance (red curve)

is good, which facilitate chip removal. However, when the tool cuts in the γ' phase, the number of potential atoms increases rapidly, as shown by b–c in Fig. 11. And the chip volume increases slowly, as shown by e–f in Fig. 11. This is due to the high elastic potential energy of the γ' phase, the workpiece is easily deformed elastically. And the soft material of the γ phase, which leads to a lower chip volume. When the tool cutting is finished, elastic recovery of the machined surface of γ' phase occurs, so the surface of γ' phase in Fig. 10a is higher than γ .

Table 4 T γ phase element content

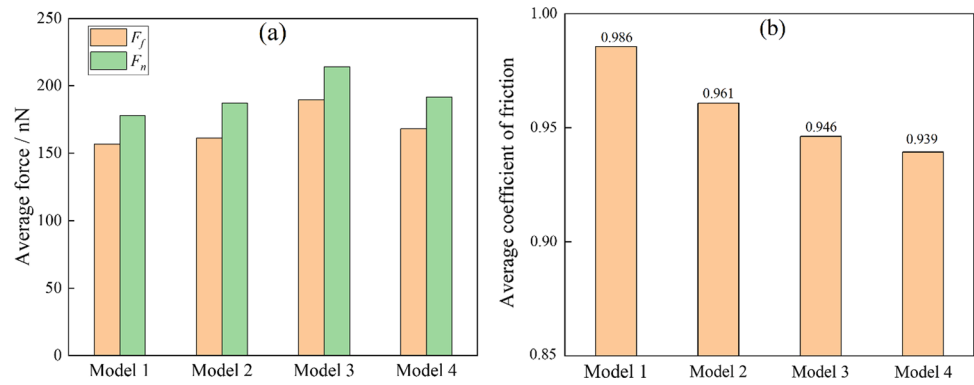
Element	Model 1 (%)	Model 2 (%)	Model 3 (%)	Model 4 (%)
Ni	100	92	82	70
Co	0	4	9	15
Cr	0	4	9	15

3.3 Cutting study after adding different contents of strengthening elements to the γ phase

To study the effect of strengthening elements on the cutting behavior of nickel-based single crystal superalloy, different contents of Cr and Co elements were added to the γ phase for cutting. The specific contents are shown in Table 4.

The average tangential and normal force are calculated for different models during the cutting process. It can be seen that the tangential force F_t and normal force F_n of Model 2–4 are larger than those of Model 1, as shown by (a) in Fig. 12. It is shown that the addition of strengthening elements can significantly increase the strength of the workpiece, leading to an increase in machining forces during cutting. However, the machining force of Model 4 is smaller than that of Model 3. This is because the addition of Cr elements, while improving the thermal corrosion performance of the alloy, also destabilizes the phases, so there is a small decrease in the strength of Model 4. However, the machining force of Model 4 is smaller than that of Model 3. This is because although the addition of the Cr element can improve the thermal corrosion performance of the alloy, it also destroys

Fig. 12 Comparison of different models **a** average force **b** friction coefficient



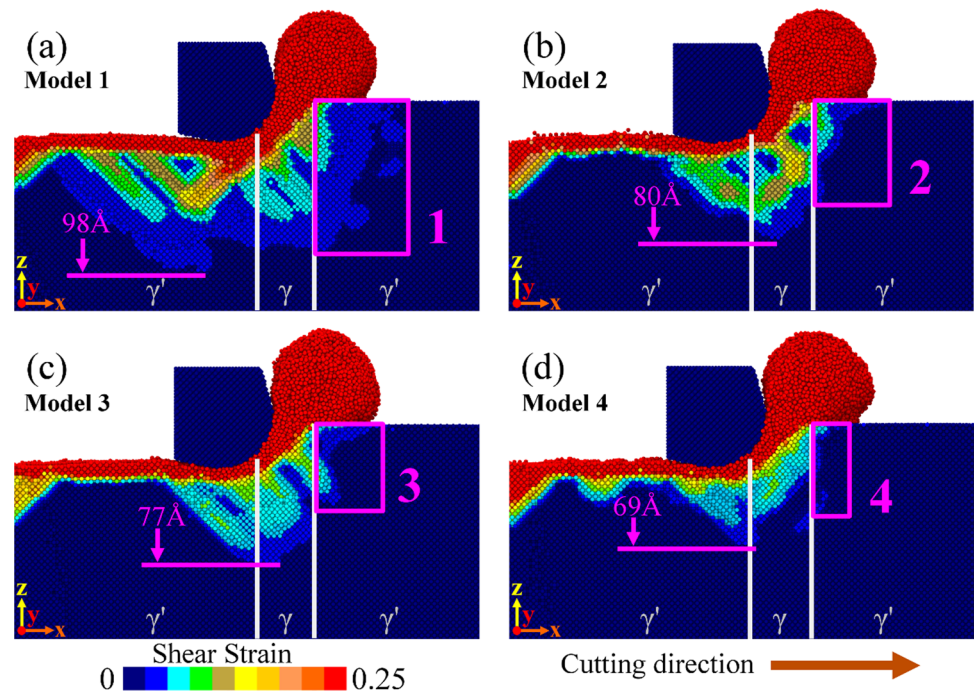
the stability of the phase, so the strength of Model 4 will have a small decrease, as shown by (b) in Fig. 11.

Figure 13 shows the shear strain distribution inside the workpiece when the four models cut to the same position of the γ phase. It can be seen that with the increase of strengthening elements, the shear strain range below the tool decreases, and the strain depth decreases. γ phase of Model 1 is pure Ni, and the lattice constants of the two phases are close to each other, so the shear strains of the two phases are very continuous during cutting, and the development of the strain region is almost not blocked by the coherent interface, as shown by 1 in Fig. 13a. After adding Cr and Co elements in γ , the coherent interface hinders the expansion of the strain region, as shown by 2 in Fig. 13b and 3 in Fig. 13c. And Model 4 with the most reinforcing elements added, the strain depth is only 69 Å, and the coherent interface has

the strongest hindrance effect on the strain region, as shown by 4 in Fig. 13d.

For the four positions in Fig. 13, the number of atoms with shear strains between 0.025 and 0.25 is counted, and the average strain value for these atoms is calculated as shown in Fig. 14. As can be seen from the histogram, the number of strains atoms in b-d decreases significantly as the workpiece is strengthened, indicating that the addition of strengthening elements can improve the deformation resistance of the workpiece. In addition, it was found that the average strain value increased as the workpiece was strengthened. This is because there are fewer atoms with low strain values inside the workpiece as the strength of the workpiece increases. In contrast, although the number of total strain atoms in model 1 is high, most of them are low-strain atoms far away from the tool, so the average strain value of model 1 is low.

Fig. 13 Subsurface atomic shear strain diagram of different models during processing



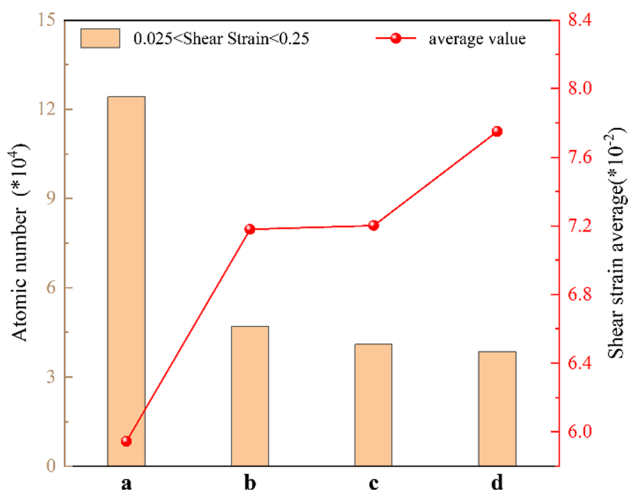


Fig. 14 Number of atoms of shear strain and average value of shear strain processed to the same position by different models

Figure 15 shows the distribution of atomic displacements inside the workpiece when the four models cut to the same position near the γ phase. The lattice constant of Ni is 3.524 Å and that of Ni₃Al is 3.561 Å. When the γ phase is pure Ni, the lattice constants of the two-phase materials are very close to each other, and the coherent interface has almost no obstruction to the displacement of the atoms. The atoms show displacement differences along the 45° direction where the FCC structure is most prone to slip, as shown by 1 and 2 in Fig. 15a. When Cr and Co elements are added to the γ phase, solid solution strengthening occurs, the displacement atom region of the workpiece will be reduced,

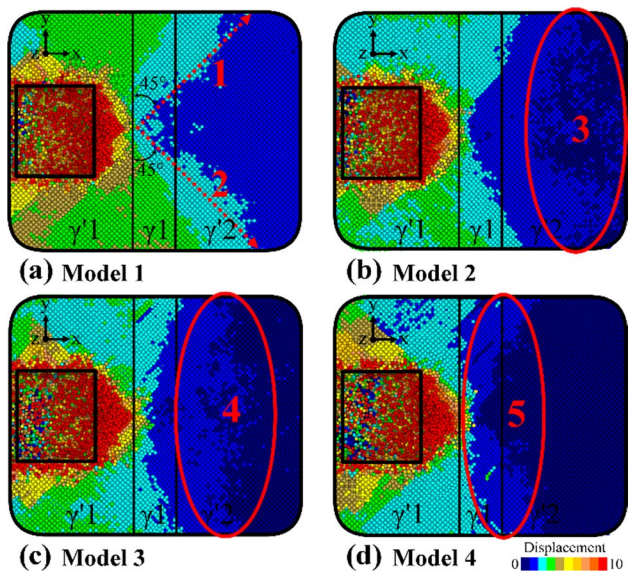


Fig. 15 Distribution of atomic displacement processed to the same position by different models

and the displacement atoms can diffuse as far as the 3 and 4 regions, as shown by (b) and (c) in Fig. 15. In the case of Model 4, which has the most reinforcing elements added, the displacement atoms will be resisted by the coherent interface and only a small number of small displacement atoms will diffuse to the next phase, as shown by 5 in Fig. 15d.

Count the number of atoms in the four positions in Fig. 15 at different displacement segments and calculate the average kinetic energy of these atoms, as shown in Fig. 16. As can be seen from the histogram, the deformation of the workpiece is dominated by displaced atoms of 1–2 Å, and the number of atomic displacements becomes smaller and smaller as the strengthening element increases. However, the kinetic energy of Model 2–4 is always greater than that of Model 1, as shown in the line graph in Fig. 16. This is because the machining force of Model 2–4 is larger than that of Model 1, and the kinetic energy generated by the workpiece is also larger. In addition, the kinetic energy of Model 4 is smaller than that of Model 3.

Figure 17 shows the comparison of the surface depth of different models after machining. It was found that the surface depth of γ phase decreased after the addition of strengthening elements, from 278.003 Å in Model 1 to 273.776 Å in Model 4, and the depth of γ phase decreased by 5.773 Å, indicating that the addition of strengthening elements would reduce the elastic recovery of γ phase and increase the material removal rate. However, the surface height of the γ' phase shows a small increase, with an increase in depth of 1.994 Å from Model 1 to Model 4.

Obtain a map of the potential energy distribution of the surfaces after machining the different models and remove the atoms with potential energy less than -3.6, as shown in Fig. 18. It is found that in Model 1, the potential energy atoms of the two phases are evenly distributed. As the content of reinforcing elements in the model increases,

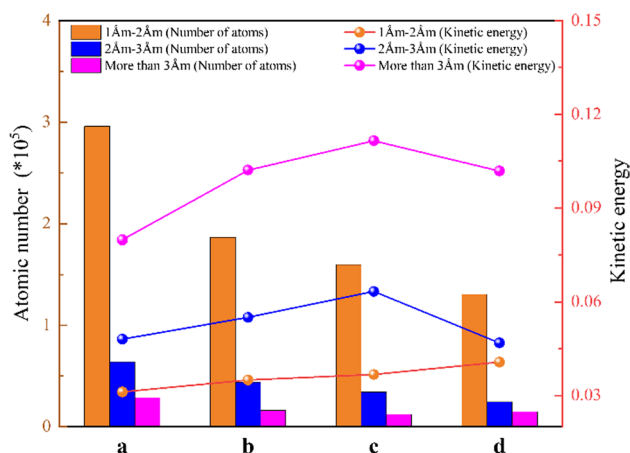


Fig. 16 Number of displaced atoms and kinetic energy of different models processed to the same location

Fig. 17 Comparison of surface depth of different models after machining

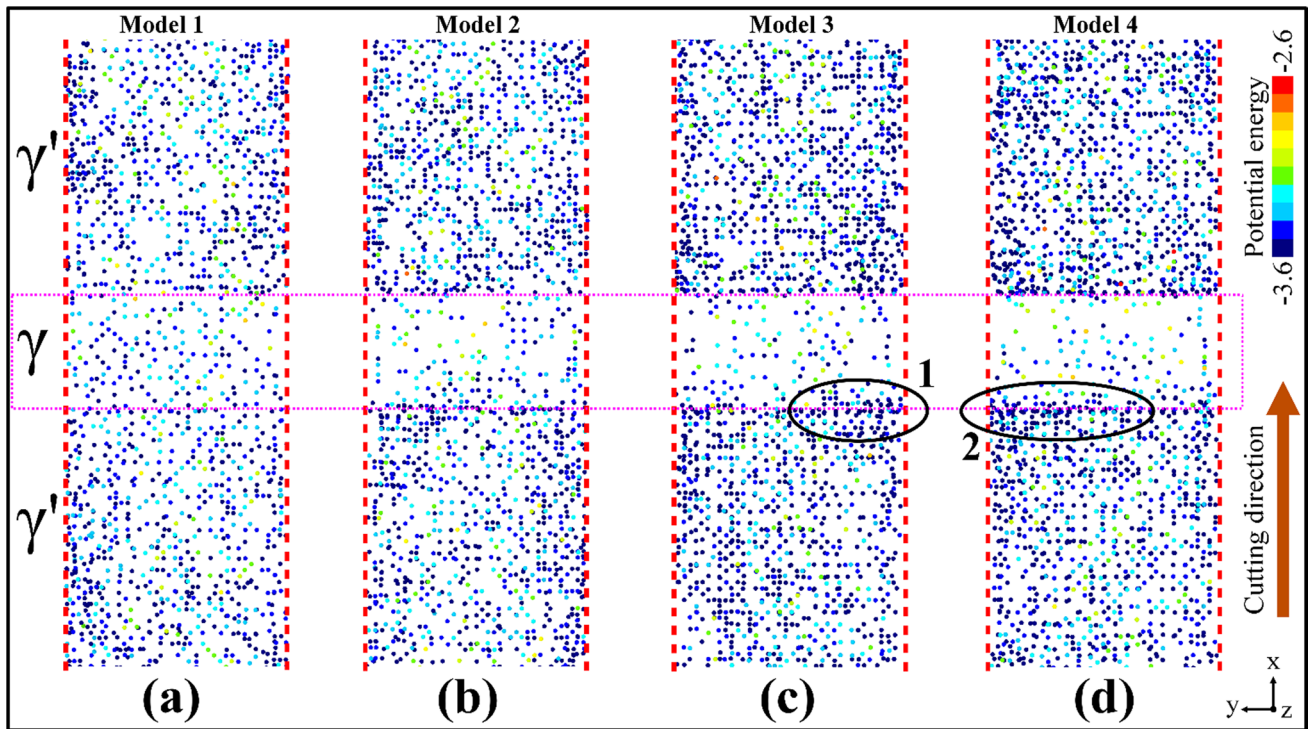
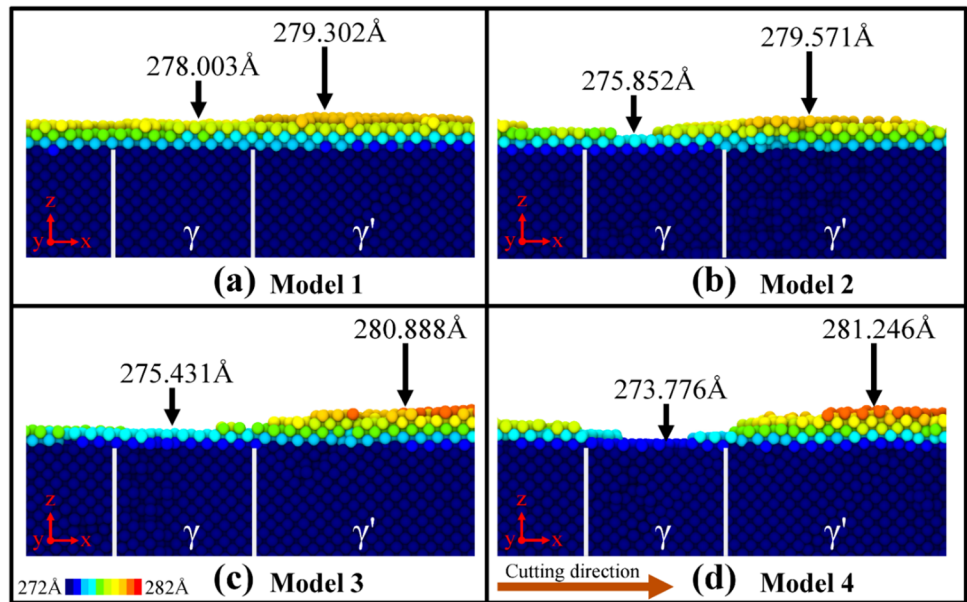


Fig. 18 Potential energy atom distribution diagram of two-phases after processing

the potential energy atoms in the γ phase decrease, but the potential energy atoms in the γ' phase increase significantly, as shown by (b), (c), and (d) in Fig. 18. It is also found that more potential energy atoms accumulate at the coherent interface in models containing more strengthening elements, as shown by 1 in Fig. 18c and 2 in Fig. 18d.

The number of atoms with potential energy greater than -3.6 in the extracted workpiece is calculated, and the density and average potential energy of these atoms in each of the two phases are shown in Fig. 19. It can be found that the number of high potential energy atoms in the γ phase is always less than in the γ' phase, and this difference

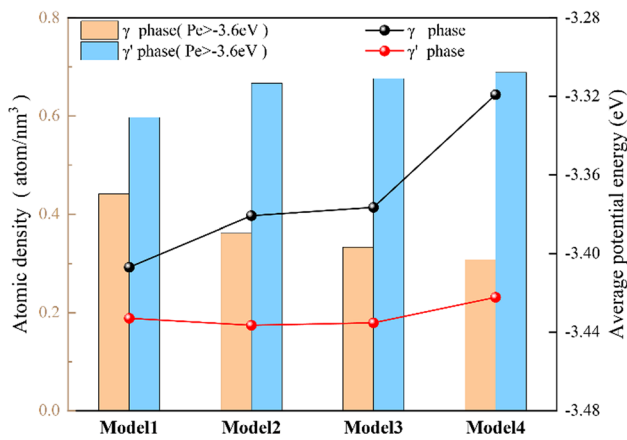


Fig. 19 Comparison of the number of potential energy atoms and the average potential energy of two-phases

becomes larger with the addition of reinforcing atoms, in addition to the average potential energy magnitude follows this pattern. The content of high potential energy atoms determines the elastic recovery of the material. A decrease in the number of potential energy atoms in the γ phase

leads to a decrease in the elastic recovery and a consequent decrease in the depth of the machined surface.

Dislocation extraction algorithm (DXA) was used to analyze the internal defects of the different models and to remove the perfectly structured FCC atoms from the crystal, as shown in Fig. 20. It can be seen that in Model 1 without reinforcing elements, the defects in two-phases are irregularly distributed, and defects such as atomic cluster, SFT, and L-C dislocations, which are common in FCC crystals, are present in the subsurface and inside the workpiece, as shown by (a) in Fig. 20. In Model 2 with a small number of reinforcing elements added, the defects in the γ phase exist in the form of dislocation tangle, as shown by b1 in Fig. 20b. As the content of strengthening elements increases, the coherent interface in Model 3 separates the defects of the two phases, and the defects of the γ' phase gradually decrease at the end of processing, as shown by 1 in Fig. 20c. The defects of the γ phase continue to exist as dislocation tangle, as shown by c1 in Fig. 20c. When there are too many Cr elements in the γ phase, the phase stability decreases, and large structural defects appear in the γ' phase, as shown by 2 in Fig. 20d.

Get the distribution of dislocation lines inside the workpiece when the tool is machined to the same position, as shown in

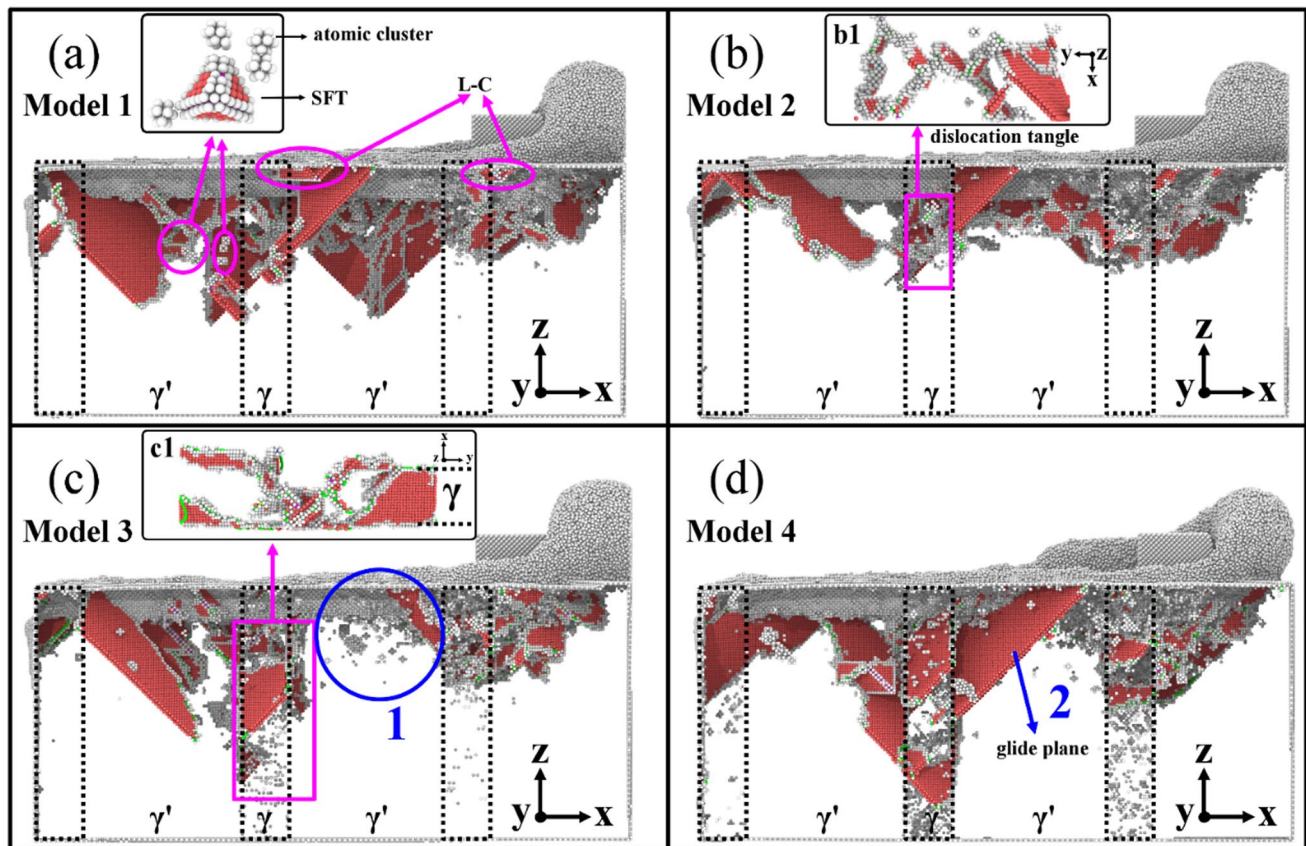


Fig. 20 Internal defects of different models. (Red atoms represent HCP atoms, and white atoms represent surface and amorphous atoms)

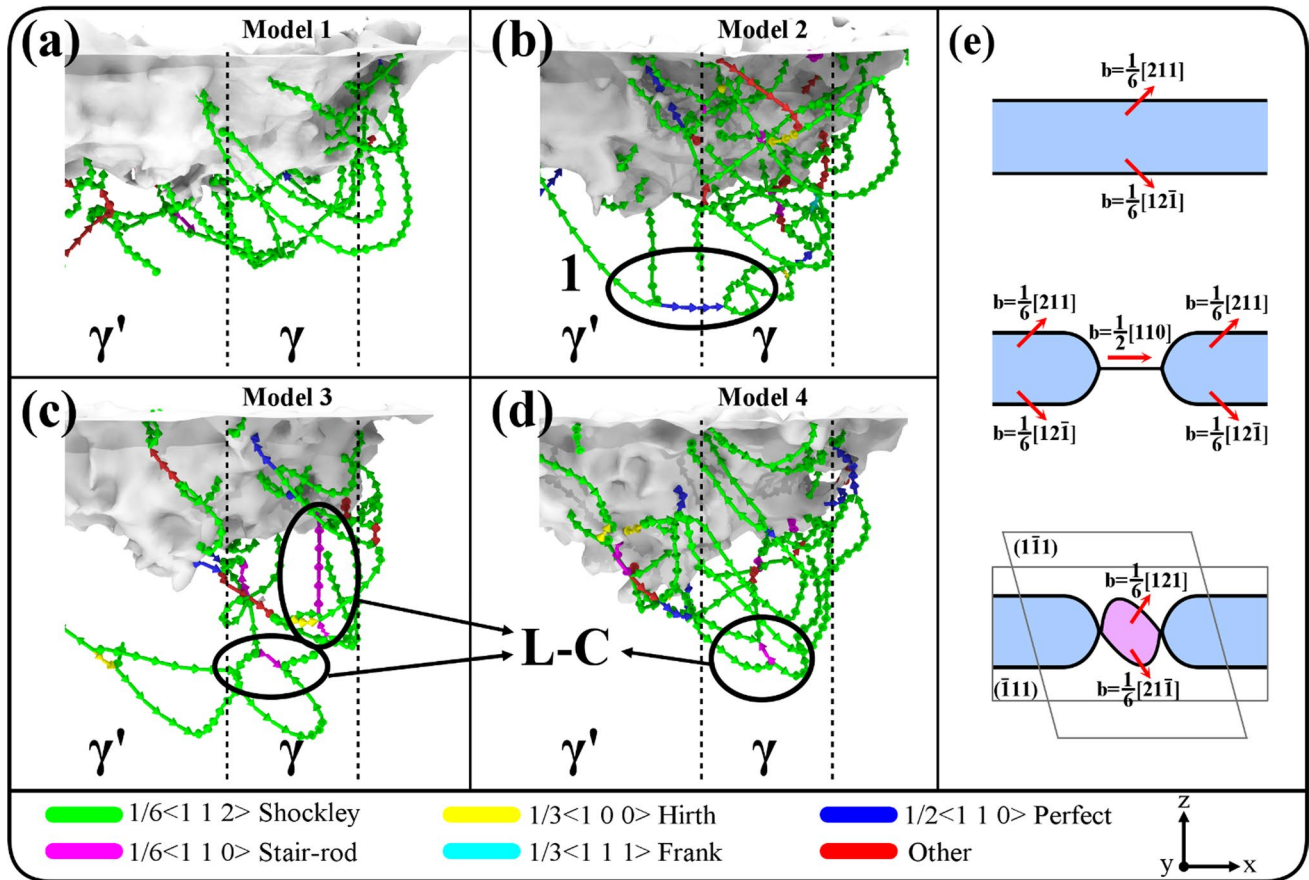


Fig. 21 a–d Nucleation, movement, and interaction of dislocations of different models during cutting; e demonstration diagram of Shockley partial dislocation collapsing and cross-slip process

Fig. 21. The cutting of the tool causes the crystal of the workpiece to slip, thus forming a fault, and two partial dislocations inevitably formed between the fault zone and the normal zone, because the whole dislocation motion in a face-centered cubic crystal is always completed by two partial dislocations. The unreinforced coherent interface does not block the development of dislocation lines, as shown by (a) in Fig. 21. When the slip process is blocked by the coherent interface, the Shockley partial dislocation on both sides of the fault will collapse into a whole dislocation, as shown by 1 in Fig. 21b. The collapsing process of extended dislocations is more likely to occur in the workpiece containing Cr and Co, because only when the energy of some positions on the fault surface increases, the extended dislocations will gradually narrow, shrink and finally become whole dislocations. The addition of reinforced atoms raises the energy of the fault surface and creates conditions for collapsing of extended dislocations. In addition, the addition of reinforcing atoms makes the γ phase more prone to L-C dislocations, as shown by (c) and (d) in Fig. 21. When the extended dislocation cross-slip, it intercepts with the L-C dislocations in the γ phase, leading to a large number of dislocation tangle in the γ phase of Model 2–4, which hinders the development

of dislocations in the workpiece and improves the deformation resistance of the workpiece. Figure 21e) shows the demonstration diagram of Shockley partial dislocation collapsing and cross-slip process.

The number of HCP atoms in the cutting process for different models is counted, as shown in Fig. 22. It was found that the HCP atomic number of the four workpieces gradually showed different growth rates after a steady increase at the beginning of the machining. The number of HCP atoms in Model 1 is always larger than that of Model 2 and Model 3, which indicates that the development of defects can be suppressed by adding reinforcing atoms in appropriate amounts. However, excessive reinforcement atoms can also destroy the stability of the workpiece, therefore, the number of defect atoms in Model 4 is larger than that of Model 2 and Model 3.

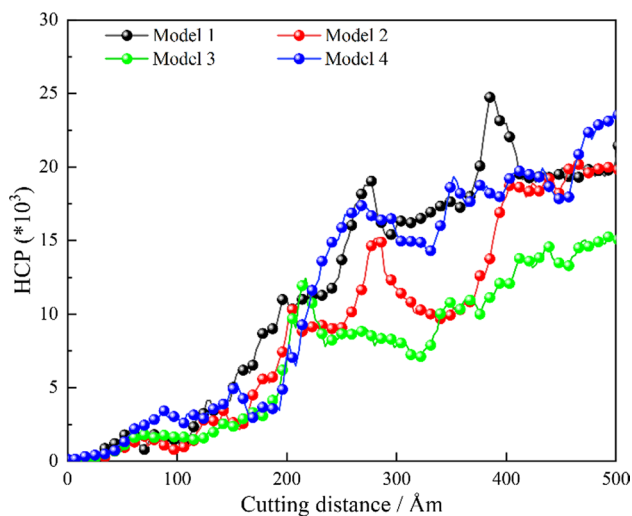


Fig. 22 Dynamic response curve of atomic number of defects with cutting distance

4 Conclusion

In this paper, the nano-machining behavior of diamond tools cutting nickel-based single crystal superalloy materials was investigated using the MD simulation method. The main results are as follows:

When cutting, the Stair-rod sessile dislocation in the γ phase and the extended dislocations in the rear meet and entangle with each other, and promote the nucleation of the small surrounding dislocations, eventually forming dislocation tangle, resulting in increased machining forces. In addition, the shear strain region of the workpiece increases when the tool cuts to the coherent interface and the γ phase and decreases when the tool cuts to the γ' phase.

The presence of a coherent interface during the cutting process improves the resistance of the workpiece to deformation. As the tool approaches the coherent interface, the displacement atoms keep accumulating in front of the coherent interface, and when the accumulated atomic energy is large enough, the coherent interface is broken and, the displacement atoms are transferred to the next phase. In addition, the strong brittleness, low potential energy and weak elastic recovery of the γ phase lead to the lowest part of the machined surface always occurring in the γ phase.

The addition of strengthening elements Cr and Co to the γ phase can improve the strength of the workpiece, leading to an increase in machining force. It also strengthens the coherent interface, which will block the expansion of the shear strain region and atomic displacement and enhance the deformation resistance of the workpiece.

As the content of strengthening elements increases, the high potential energy atoms in the γ phase during cutting will be reduced, and the elastic recovery ability will

be reduced, resulting in a lower surface depth of the γ phase. After conducting defect analysis, it is found that the strengthened workpiece is more prone to dislocation tangle in the γ phase, and dislocation entanglement can hinder the development of dislocations during machining.

Acknowledgements The work was supported by the National Natural Science Foundation of China (Grant No. 52265025).

Data Availability The data that support the findings of this study are available from the corresponding author, upon reasonable request.

Declarations

Conflict of interest We declare that we have no financial and personal relationships with other people or organizations that can inappropriately influence our work, there is no professional or other personal interest of any nature or kind in any product, service and/or company that could be construed as influencing the position presented in, or the review of, the manuscript entitled, "Atomic-scale study of the nano-cutting deformation mechanism of nickel-based single crystal superalloy containing Cr, Co and γ/γ' ".

Ethical statement We declare that our paper has not been submitted or published elsewhere; All data in this paper are true and reliable, and the main data and charts have not been published; This article does not contain plagiarism or infringement of others' intellectual property rights; This study does not involve human or animals.

References

1. W.S. Xia, X.B. Zhao, L. Yue et al., Microstructural evolution and creep mechanisms in Ni-based single crystal superalloys: a review. *J. Alloys Compd.* **819**, 152954 (2019). <https://doi.org/10.1016/j.jallcom.2019.152954>
2. S.Y. Sun, L. Li, K. He et al., Fretting fatigue damage mechanism of nickel-based single crystal superalloys at high temperature. *Int. J. Mech. Sci.* **186**, 105894 (2020). <https://doi.org/10.1016/j.ijmecsci.2020.105894>
3. Q.Q. Ding, H.B. Bei, X.B. Zhao et al., Processing, microstructures and mechanical properties of a Ni-based single crystal superalloy. *Curr. Comput.-Aided Drug Des.* **10**, 572 (2020). <https://doi.org/10.3390/cryst10070572>
4. X. Yao, Q. Ding, X. Zhao et al., Microstructural rejuvenation in a Ni-based single crystal superalloy. *Mater Today Nano.* **17**, 100152 (2022). <https://doi.org/10.1016/j.mtnano.2021.100152>
5. X.G. Wang, J.L. Liu, J.D. Liu et al., Dependence of stacking faults in gamma matrix on low-cycle fatigue behavior of a Ni-based single-crystal superalloy at elevated temperature. *Scr. Mater.* **152**, 94–97 (2018). <https://doi.org/10.1016/j.scriptamat.2018.04.020>
6. F. Wang, D. Ma, A. Bührig-Polaczke, Microsegregation behavior of alloying elements in single-crystal nickel-based superalloys with emphasis on dendritic structure. *Mater. Charact.* **127**, 311–316 (2017). <https://doi.org/10.1016/j.matchar.2017.02.030>
7. Q.Q. Ding, H.B. Bei, X. Yao et al., Temperature effects on deformation substructures and mechanisms of a Ni-based single crystal superalloy. *Appl. Mater. Today.* **23**, 101061 (2021). <https://doi.org/10.1016/j.apmt.2021.101061>
8. G.L. Wang, J.L. Liu, J.D. Liu et al., High temperature stress rupture anisotropy of a Ni-based single crystal superalloy. *J. Mater. Sci. Technol.* **32**, 1003–1007 (2016). <https://doi.org/10.1016/j.jmst.2016.08.018>

9. L. Cao, L. Yao, Y.Z. Zhou et al., Formation of the surface eutectic of a Ni-based single crystal superalloy. *J. Mater. Sci. Technol.* **33**, 347–351 (2017). <https://doi.org/10.1016/j.jmst.2016.08.014>
10. Q.H. Pan, X.B. Zhao, Y. Cheng et al., Effects of co on microstructure evolution of a 4th generation nickel-based single crystal superalloys. *Intermetallics* **153**, 107798 (2023). <https://doi.org/10.1016/j.intermet.2022.107798>
11. O. Horst, D. Adler, P. Git et al., Exploring the fundamentals of Ni-based superalloy single crystal (sx) alloy design: chemical composition vs. Microstructure. *Mater Des.* **195**, 108976 (2020). <https://doi.org/10.1016/j.matdes.2020.108976>
12. W.S. Xia, X.B. Zhao, L. Yue et al., A review of composition evolution in Ni-based single crystal superalloys. *J. Mater. Sci. Technol.* **44**, 76–95 (2020). <https://doi.org/10.1016/j.jmst.2020.01.026>
13. R. Darolia, Development of strong, oxidation and corrosion resistant nickel-based superalloys: critical review of challenges, progress and prospects. *Int. Mater. Rev.* **64**, 355–380 (2018). <https://doi.org/10.1080/09506608.2018.1516713>
14. H.B. Long, S.C. Mao, Y.N. Liu et al., Microstructural and compositional design of Ni-based single crystalline superalloys—a review. *J. Alloys Compd.* **743**, 203–220 (2018). <https://doi.org/10.1016/j.jallcom.2018.01.224>
15. Q. Gao, X.Y. Chen, Experimental research on micro-milling force of a single-crystal nickel-based superalloy. *Int. J. Adv. Manuf. Tech.* **102**, 595–604 (2019). <https://doi.org/10.1007/s00170-018-03211-x>
16. M. Cai, T. Zhu, X.J. Gao et al., Study on machining performance in grinding of Ni-base single crystal superalloy dd5. *Int. J. Adv. Manuf. Tech.* **120**, 7657–7671 (2022). <https://doi.org/10.1007/s00170-022-09256-3>
17. B. Wang, Z.Q. Liu, Y.K. Cai et al., Advancements in material removal mechanism and surface integrity of high speed metal cutting: a review. *Int. J. Mach. Tool Manuf.* **166**, 103744 (2021). <https://doi.org/10.1016/j.ijmactools.2021.103744>
18. M.A. Ia, D. Axinte, Z. Liao et al., Towards understanding the thermal history of microstructural surface deformation when cutting a next generation powder metallurgy nickel-base superalloy. *Int. J. Mach. Tool Manuf.* **168**, 103765 (2021). <https://doi.org/10.1016/j.ijmactools.2021.103765>
19. Q. Miao, W.F. Ding, J.H. Xu et al., Creep feed grinding induced gradient microstructures in the superficial layer of turbine blade root of single crystal nickel-based superalloy. *Int. J. Extreme Manuf.* **3**, 045102 (2021). <https://doi.org/10.1088/2631-7990/ac1e05>
20. J. Qiu, T. Yang, Z.Y. Zhang et al., On the anisotropic milling machinability of dd407 single crystal nickel-based superalloy. *Materials*. **15**, 2723 (2022). <https://doi.org/10.3390/ma15082723>
21. J.G. Zhang, H.X. Yuan, L.Q. Feng et al., Enhanced machinability of Ni-based single crystal superalloy by vibration-assisted diamond cutting. *Precis. Eng.* **79**, 300–309 (2023). <https://doi.org/10.1016/j.precisioneng.2022.11.012>
22. Q. Gao, P. Jin, M. Cai, Research on sub-surface recrystallization of single crystal nickel-based superalloy in micro-milling. *J. Mech Sci Technol.* **33**, 3467–3472 (2019). <https://doi.org/10.1007/s12206-019-0641-2>
23. M. Cai, Y.D. Gong, Y. Sun et al., Experimental study on grinding surface properties of nickel-based single crystal superalloy dd5. *Int. J. Adv. Manuf. Tech.* **101**, 71–85 (2018). <https://doi.org/10.1007/s00170-018-2839-3>
24. Y.C. Xu, Y.D. Gong, Z.X. Wang et al., Experimental study of Ni-based single-crystal superalloy: microstructure evolution and work hardening of ground subsurface. *Arch. Civ. Mech. Eng.* **21**, 1–11 (2021). <https://doi.org/10.1007/s43452-021-00203-9>
25. Y.M. Zhang, X.Q. Yang, X.Y. Wang et al., A micropolar peridynamic model with non-uniform horizon for static damage of solids considering different nonlocal enhancements. *Theor. Appl. Fract. Mech.* **113**, 102930 (2021). <https://doi.org/10.1016/j.tafmec.2021.102930>
26. T. Rabczuk, T. Belytschko, Cracking particles: a simplified meshfree method for arbitrary evolving cracks. *Int. J. Numer. Methods Eng.* **61**, 2316–2343 (2004). <https://doi.org/10.1002/nme.1151>
27. T. Rabczuk, G. Zi, S. Bordas et al., A simple and robust three-dimensional cracking-particle method without enrichment. *Comput. Method Appl. Mech.* **199**, 2437–2455 (2010). <https://doi.org/10.1016/j.cma.2010.03.031>
28. Y.M. Zhang, X.Y. Zhuang, Cracking elements: a self-propagating strong discontinuity embedded approach for quasi-brittle fracture. *Finite Elem. Anal. Des.* **144**, 84–100 (2018). <https://doi.org/10.1016/j.finel.2017.10.007>
29. Y.M. Zhang, X.Y. Zhuang, Cracking elements method for dynamic brittle fracture. *Theor. Appl. Fract. Mech.* **102**, 1–9 (2019). <https://doi.org/10.1016/j.tafmec.2018.09.015>
30. Y.M. Zhang, R. Lackner, M. Zeiml et al., Strong discontinuity embedded approach with standard SOS formulation: element formulation, energy-based crack-tracking strategy, and validations. *Comput. Method Appl. Mech.* **287**, 335–366 (2015). <https://doi.org/10.1016/j.cma.2015.02.001>
31. Y.M. Zhang, H.A. Mang, Global cracking elements: a novel tool for Galerkin-based approaches simulating quasi-brittle fracture. *Int J Numer Meth Eng.* **121** 2462–2480 (2019). arxiv-1908.06268
32. Y.M. Zhang, J.G. Huang, Y. Yuan et al., Cracking elements method with a dissipation-based arc-length approach. *Finite Finite Elem, Anal. Des.* **195**, 103573 (2021). <https://doi.org/10.1016/j.finel.2021.103573>
33. Y.M. Zhang, Z.R. Gao, Y.Y. Li et al., On the crack opening and energy dissipation in a continuum based disconnected crack model. *Finite Elem, Anal. Des.* **170**, 103333 (2020). <https://doi.org/10.1016/j.finel.2019.103333>
34. Y.M. Zhang, X.Y. Wang, X.Q. Wang et al., Virtual displacement based discontinuity layout optimization. *Int. J. Numer. Methods Eng.* **123**, 5682–5694 (2022). <https://doi.org/10.1002/nme.7084>
35. Y.M. Zhang, Z. Gao, X. Wang et al., Image representations of numerical simulations for training neural networks. *Cmes-Comp. Model. Eng.* **2**, 821–833 (2013). <https://doi.org/10.32604/cmes.2022.022088>
36. Y.M. Zhang, Z.R. Gao, X.Y. Wang et al., Predicting the pore-pressure and temperature of fire-loaded concrete by a hybrid neural network. *Int. J. Comput. Methods* **19**, 2142011 (2022). <https://doi.org/10.1142/s0219876221420111>
37. Y.X. Xu, M.C. Wang, F.L. Zhu et al., A molecular dynamic study of nano-grinding of a monocrystalline copper-silicon substrate. *Appl. Surf. Sci.* **493**, 933–947 (2019). <https://doi.org/10.1016/j.apsusc.2019.07.076>
38. F.F. Xu, F.Z. Fang, X.D. Zhang, Effects of recovery and side flow on surface generation in nano-cutting of single crystal silicon. *Comput. Mater. Sci.* **143**, 133–142 (2018). <https://doi.org/10.1016/j.commatsci.2017.11.002>
39. Z.P. Hao, Z.Z. Lou, Y.H. Fan, Study on the evolution mechanism of subsurface defects in nickel-based single crystal alloy during atomic and close-to-atomic scale cutting. *J. Manuf. Process.* **68**, 14–33 (2021). <https://doi.org/10.1016/j.jmapro.2021.07.013>
40. Y.H. Fan, W.Y. Wang, Z.P. Hao et al., Work hardening mechanism based on molecular dynamics simulation in cutting ni–fe–cr series of ni-based alloy. *J Alloy Compd.* **819**, 153331 (2020). <https://doi.org/10.1016/j.jallcom.2019.153331>
41. Z.P. Hao, Z.Z. Lou, Y.H. Fan, Influence of anisotropy of nickel-based single crystal superalloy in atomic and close-to-atomic scale cutting. *Precis. Eng.* **66**, 347–362 (2020). <https://doi.org/10.1016/j.precisioneng.2020.07.005>
42. Z.Z. Lou, Y.D. Yan, Y.Q. Geng et al., The effect of anisotropy of nickel-based single crystal alloys on the surface quality of

- sub-nanometer and near atomic scale cutting. *Intermetallics* **145**, 107536 (2022). <https://doi.org/10.1016/j.intermet.2022.107536>
43. Z.H. Xia, B.C. Gao, J.G. Yu et al., Molecular dynamics study of nano-cutting mechanical properties and microstructural evolution behavior of Ni/Ni₃Al phase structure. *J. Mater. Res. Technol.* **19**, 2447–2457 (2022). <https://doi.org/10.1016/j.jmrt.2022.06.021>
44. S. Plimpton, Fast parallel algorithms for short-range molecular dynamics. *J. Comput. Phys.* **117**, 1–19 (1995). <https://doi.org/10.1006/jcph.1995.1039>
45. A. Stukowski, Visualization and analysis of atomistic simulation data with Ovito—the open visualization tool. *Model. Simul. Mater. Sci. Eng.* **18**, 015012 (2010). <https://doi.org/10.1088/0965-0393/18/1/015012>
46. S.V. Hosseini, M. Vahdati, Modeling the effect of tool edge radius on contact zone in nanomachining. *Comput. Mater. Sci.* **65**, 29–36 (2012). <https://doi.org/10.1016/j.commatsci.2012.06.037>
47. Z.X. Zhu, B. Peng, R.C. Feng et al., Molecular dynamics simulation of chip formation mechanism in single-crystal nickel nanomachining. *Sci. China Technol. Sci.* **62**, 1916–1929 (2019). <https://doi.org/10.1007/s11431-019-9520-8>
48. S. Nosé, A unified formulation of the constant temperature molecular dynamics methods. *J. Chem. Phys.* **81**, 511–519 (1984). <https://doi.org/10.1063/1.447334>
49. Y.Q. Wang, S. Tang, J. Guo, Molecular dynamics study on deformation behaviour of monocrystalline GaN during nano abrasive machining - sciencedirect. *Appl. Surf. Sci.* **510**, 145492 (2020). <https://doi.org/10.1016/j.apsusc.2020.145492>
50. P.Z. Zhu, C. Qiu, F.Z. Fang et al., Molecular dynamics simulations of nanometric cutting mechanisms of amorphous alloy. *Appl Surf Sci.* **317**, 432–442 (2014). <https://doi.org/10.1016/j.apsusc.2014.08.031>
51. J. Tersoff, Modeling solid-state chemistry: interatomic potentials for multicomponent systems. *Phys. Rev. B.* **39**, 5566 (1989). <https://doi.org/10.1103/physrevb.39.5566>
52. O. Deluigi, R. Pasianot, F. Valencia et al., Simulations of primary damage in a high entropy alloy: probing enhanced radiation resistance. *Acta Mater.* **213**, 116951 (2021). <https://doi.org/10.1016/j.actamat.2021.116951>
53. M. Baskes, X. Sha, J. Angelo et al., Trapping of hydrogen to lattice defects in nickel. *Modell. Simul. Mater. Sci. Eng.* **5**, 651 (1997). <https://doi.org/10.1088/0965-0393/5/6/007>
54. S. Foiles, M. Baskes, M. Daw, Embedded-atom-method functions for the FCC metals Cu, Ag, Au, Ni, Pd, Pt, and their alloys. *Phys. Rev. B.* **33**, 7983 (1986). <https://doi.org/10.1103/physrevb.33.7983>
55. Z.P. Hao, R.R. Cui, Y.H. Fan et al., Diffusion mechanism of tools and simulation in nanoscale cutting the Ni–Fe–Cr series of nickel-based superalloy. *Int J Mech Sci.* **150**, 625–636 (2019). <https://doi.org/10.1016/j.ijmecsci.2018.10.058>
56. Z.X. Zhu, S. Jiao, H. Wang et al., Study on nanoscale friction and wear mechanism of nickel-based single crystal superalloy by molecular dynamics simulations. *Tribol Int.* **165**, 107322 (2022). <https://doi.org/10.1016/j.triboint.2021.107322>

Publisher's Note Springer Nature remains neutral with regard to jurisdictional claims in published maps and institutional affiliations.

Springer Nature or its licensor (e.g. a society or other partner) holds exclusive rights to this article under a publishing agreement with the author(s) or other rightsholder(s); author self-archiving of the accepted manuscript version of this article is solely governed by the terms of such publishing agreement and applicable law.